International Journal of Impact Engineering 75 (2015) 88–99

Contents lists available at ScienceDirect

International Journal of Impact Engineering

journal homepage: www.elsevier.com/locate/ijimpeng

Low-order modeling of vehicle impacts upon boulders embedded in cohesionless soil

M.P. Keske, A.A. Brown*, S.N. Brennan, T. Qiu

The Pennsylvania State University, University Park, PA, USA

ARTICLE INFO

Article history:
Received 22 October 2013
Received in revised form
11 July 2014
Accepted 20 July 2014
Available online 29 July 2014

Keywords:
Low-order modeling
Cohesionless soil
Vehicle impact
Boulder impact

ABSTRACT

In this paper, a planar low-order model is presented for a vehicle impact upon a boulder embedded in cohesionless soil to examine the feasibility of using boulders as anti-ram barriers. The colliding vehicle is represented as a lumped-parameter Maxwell model, the boulder is treated as a rigid body with non-negligible mass, and the soil is represented as a system of lumped-parameter Kelvin models. The low-order model allows for the linear translation of the vehicle and boulder, along with rotational motion of the boulder. The model is validated against two full scale crash tests. Both tests were performed according to ASTM F2656-07 at an M30 rating using a 6800 kg (15,000 lb.) medium-duty sized truck. The low-order model is shown to be descriptive enough for impacts that result in small boulder motion to use in sizing of boulders for use as vehicular barriers.

1. Introduction

This paper outlines an intentionally simple model for predicting the motion of a rigid, soil-embedded object like a natural or man-made boulder embedded in soil when that object is impacted by a large vehicle. The ASTM F2656-07 crash test specification with an M30 rating is the target for validation of the model, wherein the boulder is treated as an anti-ram barrier intended to prevent penetration of the impacting vehicle through the boundary of the boulder's original location. Modeling an impact between a 15,000 lb truck and a massive boulder with low-order model is challenging in large part because the boulder's ability to dissipate crash energy is dependent upon its movement through soil, which is difficult to model under dynamic loading with simple relationships.

The goal of this study is therefore to describe the energy transfer during the vehicle-boulder collision. This transfer, from vehicular kinetic energy into boulder kinetic energy, vehicle deformation, soil kinetic energy, and soil deformation, must be accurately described with a tractable set of differential equations. While modern Finite Element Analysis (FEA) impact simulation software such as LS-DYNA® has the capability to predict the results of this type of collision, these software packages are computationally expensive, simulations can take hours or days to run, and FEA approaches can obscure an understanding of fundamental physical phenomena. When selecting a natural rigid boulder as a barrier, a designer should be able to quickly iterate through embedment depths, boulder sizes, and soil conditions anticipated at the site of installation to determine the boulder's potential as an effective barrier. Therefore, a low-order model that runs rapidly on a portable computer is needed. This study derives a novel lumped-parameter, low order model from first principles relationships, and validates this model using two crash tests. The model is found to be an accurate predictor of barrier and vehicle trajectory during a collision for small angular boulder displacements. Because crash test failure standards require small displacements for a barrier to receive a passing score, the model was found to be acceptable as a rapid design iteration tool.

The concept of a low-order dynamic model for vehicular impacts on boulders embedded in cohesionless soil is a rare topic in the literature, but more general study of vehicular impacts with objects fixed to the surrounding ground, such as guardrails, is more common. A comprehensive review of FEA-based methods for modeling vehicle impacts with guardrails is presented in Ref. [1], and gives a picture of increasing levels of complexity over the years that have led to substantial improvements in accuracy in modeling vehicle impacts. In Ref. [2], FEA was used extensively to evaluate the performance of guardrails. Similarly, Wu [3] studied the dynamic deformation of guardrails through full-scale crash tests and FEA models. Naturally, in these studies, the large plastic deformation of

* Corresponding author.
E-mail address: alexanderallenbrown@gmail.com (A.A. Brown).

http://dx.doi.org/10.1016/j.ijimpeng.2014.07.010

guardrails during impacts necessitated a complex model formulation.

While guardrails are commonplace on public highways, and designed to deform substantially when impacted in order to keep vehicle occupants safe, anti-ram barriers have a different focus, placing the impetus on preventing vehicle penetration through the barrier at all costs. Recent work in predicting the behavior of man-made bollards, such as the work of Hu in Ref. [4], has also required the use of detailed FEA analysis. While not designed with vehicle occupant safety as a primary concern, steel bollards are, in general, designed to deform substantially and plastically when impacted by a vehicle. In the pages that follow, the reader will find that the present study does not require an FEA approach primarily because boulders can be approximated as rigid bodies, making the use of deformable elements to model the boulder itself unnecessary.

The remainder of the paper is organized as follows: the next section provides a brief look at prior work in soil and vehicle impact modeling without FEA, to lend context to the model development. Then, these concepts are employed along with a Newtonian first-principles derivation of the dynamic equations of motion for the boulder-soil-vehicle system. Finally, results from two full-scale crash tests are presented to compare with simulations from the low-order model. Conditions under which the model is descriptive are explored in a discussion of the experimental results.

1.1. Low-order modeling of vehicle frontal impacts

Several low-order vehicle models have been developed regarding the representation of a vehicle during a front end collision. These are briefly reviewed below in an attempt to create a low-order vehicle representation for inclusion in a descriptive model of the vehicle-barrier system.

It is common practice in literature to represent a front end vehicle collision as a 1-D Maxwell model [5]. While more complex representations of vehicle impact behavior are also present in the literature, including nonlinear spring-mass-damper systems as in Ref. [6], systems of multiple spring-mass elements as in Ref. [7], wavelet theory as in Refs. [8], and regressive time-series analysis as in Ref. [9], the well-known basic Maxwell model is used in this study for simplicity. In the following sections, this model will prove to be sufficiently descriptive of the crash behavior observed when parameters are fit to a rigid barrier impact using a finite element simulation. Shown in Fig. 1, the variables in the Maxwell Model are the effective spring constant, k_v, damping constant, c_v, lumped vehicular mass, m_v, vehicle displacement, x_v, and the displacement of the contact between the Maxwell model spring and Maxwell model damper, x'. In Ref. [5], Pawlus et al. performed a series of pole impact tests for various types of vehicles and compared the predicted displacements to measured displacements when using a Maxwell model. Pawlus then fit the spring and damper coefficients from full scale crash tests and plotted the estimated displacement, speed, and acceleration compared to the actual measurements from the vehicle. Because the values obtained for the spring and damper coefficients using the method proposed by Pawlus show

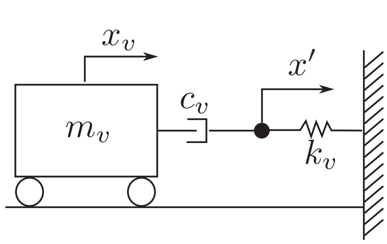

Fig. 1. Maxwell model for frontal vehicular impacts.

good agreement between predicted and measured responses of the vehicle, a Maxwell model will also be used in this work. Similar to Pawlus et al.'s work, the values obtained for the Maxwell model parameters in the present study are compared against full scale crash tests in the experiments that follow. However, because the vehicle-boulder impact under consideration in this study cannot be reliably considered analogous to a rigid pole impact, a suitable model for the soil's reaction to both static and dynamic loading is also needed.

1.2. Static analysis of laterally loaded piles

Zhang [10] developed a computational method for predicting the displacement of a laterally loaded, short rigid pile in cohesionless soil due to static loading. For small displacements, short rigid piles were assumed to rotate about a single point. Rather than representing the soil as a system of nonlinear springs and using explicitly measured pressure–displacement curves in the prediction of pile motion, Zhang calculated the soil reaction pressure as a function of embedment depth and static forces. In Zhang's work, the predicted pile displacements agreed well with experimental data. The methodology presented does not, however, account for explicit pile translation or the effect of pile inertial properties such as mass moment of inertia, primarily because Zhang assumes static loading conditions. Nevertheless, Zhang's determination of ultimate lateral loads for cohesionless soils and the corresponding relationship between the embedment depth and the ultimate soil lateral load are used in the present study as pieces of the model for soil-boulder interaction.

1.3. Dynamic analysis for laterally loaded piles

Naggar and Bentley [11] developed a method for predicting the displacements of a laterally loaded, long elastic pile under dynamic loading. The methodology proposed incorporated the p–y method applied to a Winkler model as well as wave propagation and energy dissipation to develop static p–y curves. Then, the static p–y curves were transformed into dynamic p–y curves through the addition of dampers. The mass of the soil within the inner field was lumped against the pile due to the assumed massless area as demonstrated by Novak and Sheta [12]. In Ref. [11], Naggar and Bentley calculated the spring and dashpot constants for the soil element based on empirical data from cyclic pile head loading tests for specific soils. Those spring and dashpot constants were then used to predict the displacement of a dynamically laterally loaded pile. They also compared the predicted pile head displacements against measured pile head deflections for two cases of dynamically, laterally loaded, long elastic piles using a "statnamic" device, which incorporates both static and dynamic loading. The two cases involved a lateral dynamic load of 350 kN and 470 kN respectively. Further soil and pile conditions of the tests can be found in Ref. [13].

The methodology proposed in Ref. [11], however, determines the soil damping explicitly through experiments and curve fitting. It is the goal of this work, rather, to develop a theoretical model using a minimal number of empirical relations. Additionally, the methodology in Ref. [8] was developed for long elastic piles whereas this work is limited to short rigid boulders. The inclusion of soil damping to create a set of dynamic p–y curves as well as the lumped soil mass against the pile are used in this work in the modeling of boulder motion in soil.

2. Low-order model development

This section presents the development of a low-order model for a vehicle impact upon a boulder embedded in cohesionless soil such as sand or gravel. From this model, it is possible to not only predict vehicle and boulder motion but also suitability of the boulder for use as a vehicle anti-ram barrier. This model is developed as a combination of commonly used vehicle and pile models, and will capture both motion of the vehicle as well as motion of the boulder. Finally, a method for simulating the results of various model parameters is presented.

2.1. Coordinate systems and nomenclature

The global coordinate used throughout this study is oriented such that the X direction is to the right, the Y direction is down, and the Z direction is into the page. All displacements and corresponding time derivatives along the X axis are noted as x, $\dot{x}$, … etc., and all rotational displacements about the Z axis are noted as θ, $\dot{\theta}$, … etc. The motion of the vehicle is assumed to be one dimensional in the positive X direction. The variable x_v is the X direction displacement of the vehicle with respect to the global reference frame.

Similar to the motion of the vehicle, the boulder is assumed to translate solely in the positive X direction and independently rotate about the Z axis as illustrated in Fig. 2. The variables in Fig. 2 are the X direction displacement of the center of mass of the boulder-soil subsystem, x_b, and the angle of rotation of the boulder-soil subsystem about the Z axis, θ_b. It should be noted that the center of mass of the boulder and soil system is not the same as the center of mass for the boulder alone, but the system's center of mass is the displacement simulated by the equations developed in this study.

It is assumed throughout this study that the length, L, width, W, and height, H, of the boulder are such that the length is always parallel to the direction of impact in the XY plane, the width is perpendicular to the direction of impact in the XZ plane, and the height is in the YZ plane. Fig. 2 illustrates a typical scenario for a vehicle impact upon a soil-embedded barrier. The variable d in Fig. 2 is the embedment depth of the boulder.

2.2. Model development

The low-order model presented in this study is a combination of a lumped-parameter vehicle model, a rigid body representing the boulder, and a lumped-parameter soil model consisting of individual masses and nonlinear springs and dampers representing the affected soil during vehicular impact. The model presented considers only in-plane motion and as such is only a quasi-3D model, a simplification justified by the test results presented in the Validation section. As presented in Ref. [5], the use of a lumped-parameter Maxwell model is most aptly used for collisions in which a relatively large amount of crush is observed. Fig. 2 shows the low-order model as presented using a lumped-parameter Maxwell model for the vehicle.

There are three degrees of freedom for the low-order model: the displacement of the vehicle, x_v, displacement of the boulder-soil subsystem, x_b, and the rotation of the boulder-soil subsystem, θ_b.

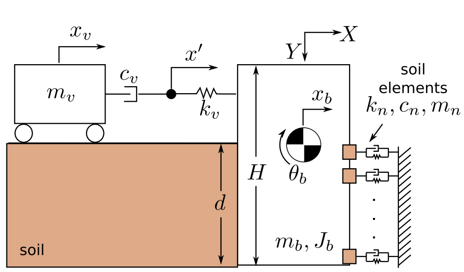

Fig. 2. Low-order model for vehicle impacts upon boulders embedded in soil.

As seen in literature, the soil surrounding a laterally loaded pile can be represented as a system of nonlinear springs and dampers [13]. As presented by Kim in Ref. [14], the general shape of affected soil surrounding the boulder during lateral loading can be found using the effective angle of internal friction of the soil and the embedded pile or boulder geometries. Similarly, in the derivation that follows the overall shape of the soil wedge after the soil fails in shear is found from the shear plane of the soil as defined by Ref. θ_w in Fig. 3, and defined in Equation (1).

$$\theta_w = \frac{\pi}{4} + \frac{\phi'}{2}, \tag{1}$$

where ϕ' is the soil's angle of internal friction. This “shear wedge” is used in part to calculate the mass of each soil element shown in Fig. 3 ϕ' defines a second soil wedge used to approximate a “compression region” in the soil in front of the boulder, which will be used in deriving equivalent soil spring constants in the model development that follows. The lengths of these soil wedges along the ground plane are denoted by $L_{\text{soil},m}$ and $L_{\text{soil},c}$ respectively. The first is used in determining the “fixed mass” of each soil element, which remains constant after the soil fails in shear, and the second is used in determining an effective spring constant for each soil element to use in the idealized spring of the Kelvin model for each element.

The true three-dimensional boulder-soil subsystem is simplified by considering only the soil directly behind the boulder, marked in Fig. 3. The soil in Fig. 3 is discretized into N evenly distributed elements, and modeled as a system of springs and dampers. Similar to the work of Naggar and Bently [11], the mass of the soil elements are lumped against the boulder and attached to the springs and dampers such that the springs and dampers are in parallel. The variable $L_{\text{soil},m}$ in Fig. 3 is the original length of the soil wedge used to calculate soil element mass, and the variable h_e is the height of a single soil element. Each soil element is assumed to have a trapezoidal cross-section where the mass of the nth soil element, m_n, is found using Equation (2).

$$m_n = \rho_{\text{soil}} W h_e \tan\theta_w \left[d - h_e\left(n - \frac{1}{2}\right)\right] \tag{2}$$

where ρ_{soil} is the mass density of the soil. It is assumed that the springs and dampers representing the soil do not undergo rotation and act solely in the x-direction.

A free body diagram of the boulder-soil subsystem is shown in Fig. 4. The force exerted on the boulder from the vehicle, F_v, is applied at an eccentricity e above the soil line. Additionally, a restoring moment due to gravity, M_r, is added to the boulder because the mass of the boulder is non-negligible. The friction acting on the boulder from the surrounding soil is neglected, as in Zhang [10]. Fig. 4 shows the center of mass in the X-direction as

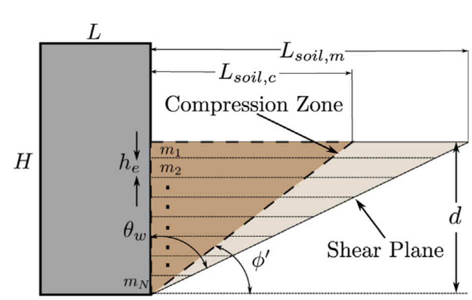

Fig. 3. Idealized 2-D wedge shape based on 3-D soil wedge geometry divided into a discrete set of Kelvin models.

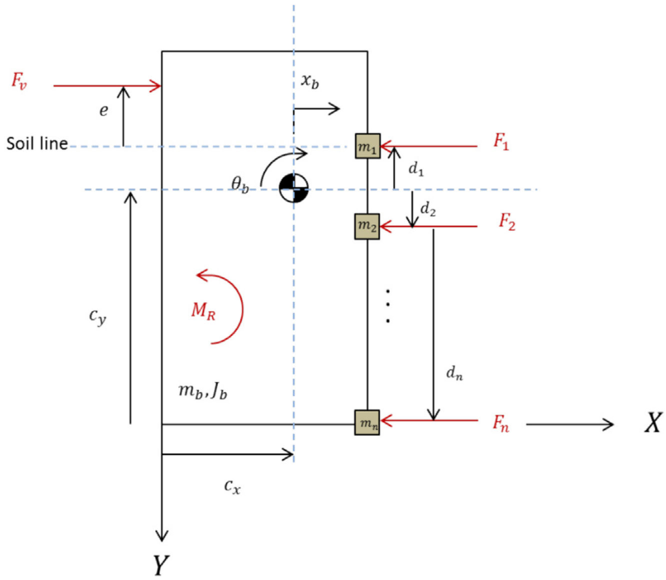

Fig. 4. Free body diagram of the boulder-soil subsystem.

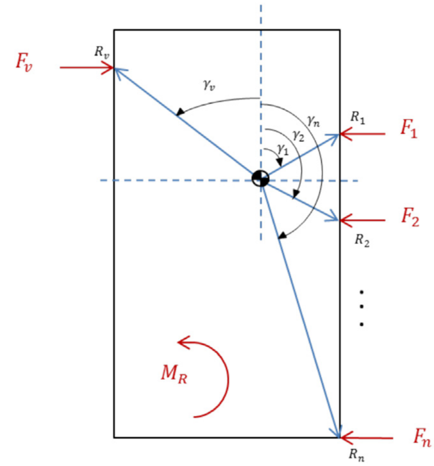

Fig. 5. Secondary free body diagram of the boulder-soil subsystem.

measured from the lower left corner as c_x, the center of mass in the Y-direction as measured from the lower left corner of the boulder as c_y, the depths of each soil layer below the center of mass of the boulder-soil subsystem as $d_1, d_2, \ldots, d_N$, the mass of the boulder m_b, and the mass moment of inertia of the boulder about the center of mass of the boulder-soil subsystem as J_b.

The center of mass for the boulder-soil subsystem as measured with respect to the local origin in the X-direction is found using Equation (3).

$$c_x = \frac{1}{\left(\sum\limits_{n=1}^{N} m_n\right) + m_b} \left[\left(\sum_{n=1}^{N} m_n\right) L + m_b \frac{L}{2}\right] \tag{3}$$

and the center of mass for the boulder-soil system as measured with respect to the local origin in the Y direction is found using Equation (4).

$$c_y = \frac{1}{\left(\sum\limits_{n=1}^{N} m_n\right) + m_b} \cdot \left[\left(\sum_{n=1}^{N} m_n d \frac{-\left(n - N - \frac{1}{2}\right)}{N}\right) + m_b \frac{H}{2}\right] \tag{4}$$

As a means of rapidly calculating moments, additional coordinates are employed as in Fig. 5, which shows the radial distance from the boulder-soil center of mass to the impact point of the vehicle as R_v, the radial distances from the boulder-soil center of mass to the soil elements as R_n, the angle measured from vertical to the vehicle impact point as γ_v, and the angles measured from vertical to the soil elements as γ_n. These quantities are given by Equations (5)–(8) below.

$$\gamma_v = \arctan \frac{c_x}{e + d_1} \tag{5}$$

$$R_v = \sqrt{(e + d_1)^2 + c_x^2} \tag{6}$$

$$\gamma_n = \arctan\left(\frac{d_n}{(L - c_x)}\right) + \frac{\pi}{2} \tag{7}$$

$$R_n = \sqrt{d_n^2 + (L - c_x)^2} \tag{8}$$

The eccentricity of the vehicle impact is computed by treating the force from the vehicle as an evenly distributed load across the impact area on the face of the boulder, as shown in Fig. 6. In terms of the boulder's reaction, the distributed load is consolidated into an equivalent point load. Fig. 6 shows the distance from the ground to the bottom of the vehicle bumper as e_{bumper}, and the distance from the ground to either the top of the boulder or to the top of the vehicle hood as e', along with the eccentricity of the equivalent point load F_v as e. The eccentricity e is calculated as in Equation (9).

$$e = \frac{1}{2}\left(e' + e_{\text{bumper}}\right) \tag{9}$$

2.3. Boulder-soil subsystem governing equations of motion

Applying Newton's second law to the mass shown in Fig. 4 yields Equations (10) and (11).

$$m_{\text{eff}} \ddot{x}_b = \sum_{n=1}^{N} \{F_n\} + F_v \tag{10}$$

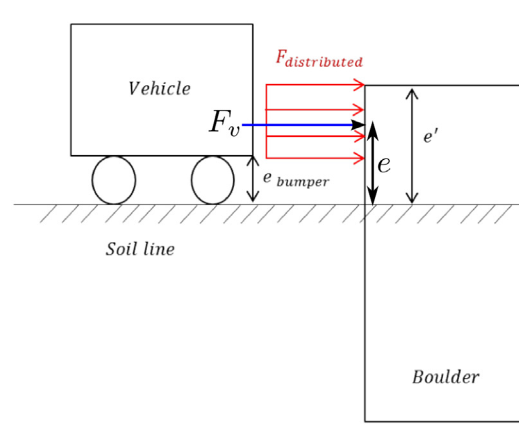

Fig. 6. Eccentricity of vehicle impact force from distributed load.

$$J_{\text{eff}}\ddot{\theta}_b = \sum_{n=1}^{N}\{M_n\} + M_v + M_r \tag{11}$$

where m_{eff} and J_{eff} are the effective mass of the boulder-soil subsystem and the mass moment of inertia of the boulder-soil subsystem about the system's center of mass, given by Equations (12) and (13).

$$m_{\text{eff}} = \left(m_b + \sum_{n=1}^{N}\{m_n\}\right) \tag{12}$$

$$J_{\text{eff}} = \left(J_b + \sum_{n=1}^{N}\left\{m_n\left(d_n^2 + l_n^2\right)\right\}\right) \tag{13}$$

where l_n is the distance in the X-direction from the center of mass of the boulder-soil subsystem to the soil elements, and given by Equation (14).

$$l_n = L - c_x \tag{14}$$

The mass of the boulder, m_b, is found using Equation (15).

$$m_b = \rho_{\text{boulder}}\text{LWH} \tag{15}$$

where ρ_{boulder} is the mass density of the boulder, and the mass moment of inertia of the boulder about the mass center is found using Equation (16).

$$J_b = \frac{1}{12}m_b\left(\left(\frac{H}{2}\right)^2 + \left(\frac{L}{2}\right)^2\right) + m_b\left(\left(c_y - \frac{H}{2}\right)^2 + \left(c_x - \frac{L}{2}\right)^2\right) \tag{16}$$

Similar to the boulder-soil subsystem, a free body diagram can be constructed for the lumped-parameter Maxwell vehicle model. It is assumed that there is no slip at the contact point between the vehicle and the boulder. Applying Newton's second law to the lumped-parameter Maxwell model in Fig. 2 yields Equation (17) and Equation (18).

$$m_v\ddot{x}_v = -F_v' \tag{17}$$

$$F_v' = F_v \tag{18}$$

Here, F_v' is the equivalent Maxwell model damping force, and F_v is the equivalent Maxwell model spring force.

2.4. Derivation of soil forces and resulting moments

As presented in Ref. [11], the springs and dampers representing the soil in Fig. 3 are placed in parallel; thus, the N soil forces are found using Equation (19) below:

$$F_n = -\left(F_{k_n} + F_{c_n}\right) \tag{19}$$

where F_{k_n} is the force from the nth soil representative spring and F_{c_n} is the force from the nth representative damper, with sign conventions defined relative to the boulder-soil subsystem displacement x_b. The N moments resulting from the soil forces are found using Equation (20).

$$M_n = -F_nR_n\cos(\gamma_n + \theta_b - \pi) \tag{20}$$

The soil representative spring forces F_{k_n} in Equation (19) are found using Equation (21).

$$F_{k_n} = k_n\Delta x_n \tag{21}$$

where Δx_n is the linear displacement in the X-direction of the nth soil mass element and k_n is its effective spring constant. Since the boulder is assumed to undergo rigid body motion, each x_n can be related geometrically to the lateral position of the boulder, x_b, and the angle of rotation of the boulder, θ_b using Equation (22).

$$\Delta x_n = x_b + R_n\sin(\gamma_n + \theta_b) - R_n\sin(\gamma_n) \tag{22}$$

The spring constants for the soil elements are found by idealizing each element as a long, slender rod. The equivalent spring constant of each of these rods is approximated using the basic stress–strain compressive relationship for a long slender rod as in Equation (23).

$$k_{\text{rod}} = \frac{E_{\text{rod}}A_{\text{rod}}}{L_{\text{rod}}} \tag{23}$$

where E_{rod} is the Young's modulus of the rod material, A_{rod} is the cross-sectional area of the rod, and L_{rod} is the length of the rod. Applying this to the idealization of each soil element yields Equation (24).

$$k_n = \frac{1\cdot 10^6\beta dW}{L_{\text{soil},c}N}\alpha_n \tag{24}$$

where β is the constant of horizontal subgrade reaction of the soil in $\frac{\text{MN}}{\text{m}^2}$, $L_{\text{soil},c}$ is an estimate of the original soil "compression region" wedge length, and α_n is the depth of the soil elements from the soil line to the bottom of the boulder in the range $(\frac{d}{2N}, \frac{d}{N}, d(1-\frac{1}{2N}))$. As defined in Fig. 3, the length of the compression soil wedge, $L_{\text{soil},c}$, is found using the simple geometric relationship in Equation (25).

$$L_{\text{soil},c} = \frac{d}{\tan\phi'} \tag{25}$$

With the definition of ϕ', this equation is consistent with [15]. With Equation (25), the equivalent soil spring exerts a force on the boulder according to Equation (26), which is obtained by substituting Equation (25) into Equation (24).

$$F_{k_n} = \frac{1\cdot 10^6\beta W\tan\phi'}{N}\alpha_n\cdot[x_b + R_n\sin(\gamma_n + \theta_b) - R_n\sin(\gamma_n)] \tag{26}$$

An ultimate lateral resistance, however, exists for soil at a given depth. For 2-D static problems (e.g., retaining walls), the ultimate lateral resistance is provided by the passive earth pressure, which is well established in geotechnical engineering (e.g., Terzaghi et al. in Ref. [16]). For the boulder-soil subsystem, however, the 3-D effects of soil displacement ahead of the boulder should be considered to determine the ultimate lateral pressure available to each soil element in this simplified 2-D model. Based on the work of Fleming et al. [17], Zhang et al. [18], Guo [19], and Zhang [10] on laterally loaded rigid piles in cohesionless soils, the ultimate lateral pressure, σ_n for each laterally loaded soil element can be estimated using Equation (27).

$$\sigma_n = K_p^2\rho_{\text{soil}}g\alpha_nK_\varepsilon \tag{27}$$

Here, $K_p = \tan^2(\frac{\pi}{4} + \frac{\phi'}{2})$ is the Rankine passive earth pressure coefficient, g is the gravitational constant, and K_ε is a constant that reflects the strain-rate effect on soil resistance. The effect of strain rate on the stress-strain behavior of cohesionless soil has been studied by various researchers as summarized by Yamamuro et al. [20]. Under strain rates of up to $1000\frac{\%}{s}$, an increase in shear strength by approximately 15–20% more than the static values was generally observed (e.g., Seed and Lundgren [21]; Lee et al. [22]). For simplicity and conservative selection of boulders to serve as effective vehicular barriers, the strain-rate effect on the soil resistance is neglected in this study (i.e., $K_\varepsilon = 1$). The ultimate lateral force provided by each soil element is thus given by Equation (28).

$$F_{u_n} = \sigma_n A_n = K_p^2 \rho_{\text{soil}} g \alpha_n K_\varepsilon \frac{Wd}{N} \tag{28}$$

This expression for the ultimate resistive force produced by each soil element under compression is used in the subsequent simulations to prevent the “spring effect” of each soil element from providing more force than is physically possible.

Although the low-order model lumps the discretized soil elements against the boulder, the damping constant for the representative soil dampers is derived analytically by applying the conservation of momentum to the boulder-soil subsystem as the boulder plows through the soil during a vehicle impact. Since the low-order model assumes that all translations of the soil elements are purely in the X-direction, the sum of the forces acting on the boulder from the soil elements is found using the momentum transfer formulation of Newtonâ€™s law:

$$\frac{d\overrightarrow{P}_n}{dt} = \sum \overrightarrow{F_n} = (m_n + m_n')\ddot{x}_n + (\dot{m}_n + \dot{m}_n')\dot{x}_n \tag{29}$$

where $\overrightarrow{P}_n$ is the momentum of the nth soil element, m_n' is the accumulated mass of the nth soil element as the boulder plows through the soil, $x_6 = \dot{x}_v \quad \dot{x}_6 = x_7$ is the time derivative of the lumped soil masses defined in Fig. 3, and $\dot{m}_n'$ is the time derivative of the accumulated mass of the nth element. Since it is assumed that the soil masses lumped against the boulder do not change with respect to time, $\dot{m}_n$ is assumed zero. Accumulated mass can be calculated by sweeping the soil element swept area across the forward distance traveled by each soil element:

$$m_n' = \rho_{\text{soil}} A_n x_n \tag{30}$$

and the time derivative of the accumulated mass is therefore given by Equation (31).

$$\dot{m}_n' = \rho_{\text{soil}} A_n \dot{x}_n \tag{31}$$

Substituting Equation (31) into Equation (29) and setting $\dot{m}_n$ equal to zero yields Equation (32).

$$\frac{d\overrightarrow{P}_n}{dt} = \sum \overrightarrow{F_n} = (m_n + m_n')\ddot{x}_n + \rho_{\text{soil}} A_n \dot{x}_n^2 \tag{32}$$

This equation resembles the equation for fluid drag, and can thus be rewritten conveniently as in Equation (33).

$$\frac{d\overrightarrow{P}_n}{dt} = \sum \overrightarrow{F_n} = (m_n + m_n')\ddot{x}_n + c_n \dot{x}_n^2 \tag{33}$$

Here, c_n is the “effective drag coefficient” of the soil. Thus, the analysis performed for a boulder during a vehicle impact uses damper elements for soil that provide a resistive force proportional to velocity squared, and the drag coefficients c_n are functions of the element swept area and soil density. This type of damping captures the physics of the momentum transfer between the boulder and the soil mound that accumulates in front of each moving mass element. In testing the effects of various model assumptions on resulting rock behavior, the authors noticed that velocity-squared damping produces a much better model fit than a linear damping model.

In the differential equation for the motion of the boulder-soil subsystem, Equation (10), the soil damping forces are given by:

$$F_{c_n} = c_n \dot{x}_n^2 \text{sign}(\dot{x}_n) \tag{34}$$

Similar to the linear displacement of each soil element, the X-velocity of each soil element can be related to the planar angular velocity of the boulder using Equation (35).

$$\dot{x}_n = \dot{x}_b + \dot{\theta}_b R_n \cos(\gamma_n + \theta_b) \tag{35}$$

With simple substitutions, the final equation for the damping force contributed by each soil element is shown in Equation (36).

$$F_{c_n} = \frac{\rho_{\text{soil}} Wd}{N}\left(\dot{x}_b + \dot{\theta}_b R_n \cos(\gamma_n + \theta_b)\right)^2 \cdot \text{sign}\left(\left[\dot{x}_b + \dot{\theta}_b R_n \cos(\gamma_n + \theta_b)\right]\right) \tag{36}$$

Because the pile geometries in Ref. [10] were slender, Zhang neglected the restoring moment which resists tipping of a rigid body due to corner ground reaction forces. The restoring moment acting on the boulder during a vehicle impact is calculated such that it is equal in magnitude and opposite in direction to the sum of all other moments acting on the boulder until the maximum restoring moment due to gravity is achieved. Calculating the restoring moment in the aforementioned manner allows for zero boulder rotation in the event that the vehicle does not enact a large enough moment to cause the boulder to tip. Since it is also assumed that the boulder-soil subsystem center of mass does not translate in the Y-direction, the maximum restoring moment due to gravity acting on the boulder is first estimated under the two cases shown below:

$$\text{for } \dot{\theta}_b > 0; \quad M_{R,\max} = -\text{sign}(\sin(\gamma_N + \theta_b)) \cdot m_b g R_N \cos(\gamma_N + \theta_b) \tag{37}$$

$$\text{for } \dot{\theta}_b \le 0; \quad M_{R,\max} = 0 \tag{38}$$

The estimated restoring moment is compared to the sum of the moments on the boulder such that:

$$M_R = -\text{sign}(\sin(\gamma_N + \theta_b))\left[\sum_{n=1}^{N}\{M_n\} + M_v\right], \quad \text{for}\left(M_v + \sum_{n=1}^{N}\{M_n\}\right) \ne 0 \tag{39}$$

The absolute value of the restoring moment is then limited such that it cannot exceed the absolute value of the estimated maximum restoring moment calculated in Equation (37). If the calculated value exceeds this maximum, it is simply set as the maximum theoretical restoring moment.

With a suitable description of the motion of the boulder in response to forcing by the vehicle impact, including a physics-based model of soil resistive forces, all that remains is to link the vehicle's inertia properties and initial velocity to the interaction forces between the boulder and the vehicle chassis. As mentioned earlier, this coupling is achieved by considering a Maxwell model of the vehicle crush zone.

2.5. Derivation of vehicle force based on a lumped-parameter Maxwell model

The governing equations for the Maxwell model as defined by Fig. 2 are shown in Equations (40) and (41).

$$m_v \ddot{x}_v = -F_v' = -c_v\left(\dot{x}_v - \dot{x}'\right) \tag{40}$$

Fig. 7. Aerial view of the Larson Institute Crash Safety Research Facility at Penn State.

$$0 = F_v' - F_v = c_v\left(\dot{x}_v - \dot{x}'\right) - k_v\left(x' - \delta x_{bv}\right) \tag{41}$$

where δx_{bv} is the change in linear displacement between the vehicle and the contact point of the vehicle on the boulder. Differentiating Equations (40) and (41) with respect to time yields:

$$m_v \dddot{x}_v = -c_v(\ddot{x}_v - \ddot{x}') \tag{42}$$

$$0 = c_v(\ddot{x}_v - \ddot{x}') - k_v\left(\dot{x}' - \dot{x}_{bv}\right) \tag{43}$$

Summing Equations (42) and (43), and solving for the velocity $\dot{x}'$ yields Equation (44).

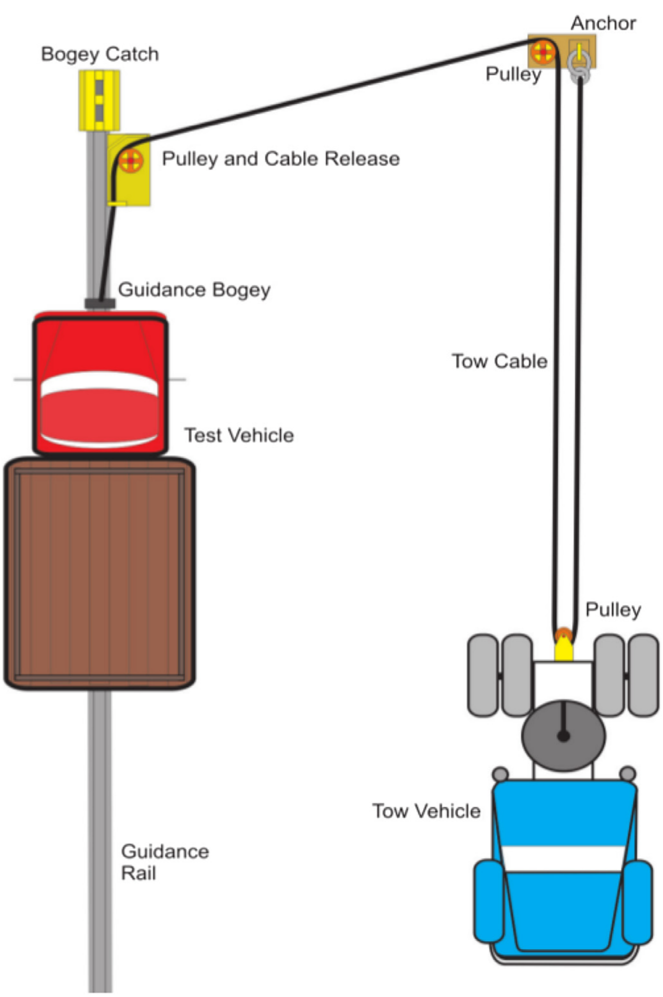

Fig. 8. Crash Safety Research Center crash test towing system.

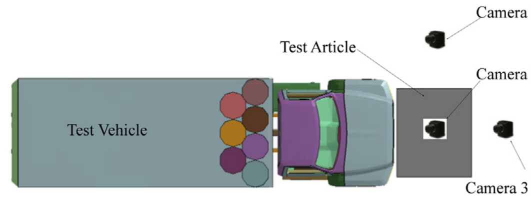

Fig. 9. Location of high-speed video cameras during field test (not to scale).

$$\dot{x}' = -\frac{m_v \dddot{x}_v}{k_v} + \dot{x}_{bv} \tag{44}$$

Finally, assembling Equations (44) and (40) results in the final governing equation for the lumped-parameter Maxwell vehicle model in Equation (45).

$$\dddot{x}_v + \frac{k_v}{c_v}\ddot{x}_v + \frac{k_v}{m_v}\dot{x}_v = \frac{k_v}{m_v}\left[\dot{x}_b + \dot{\theta}_b R_v \cos(\gamma_v + \theta_b)\right] \tag{45}$$

The force at the contact between the Maxwell model spring and Maxwell model damper must be equal. This in turn must equal the force acting on the boulder during an impact. Therefore, consider the following statement of equivalence:

$$F_v = F_v' \tag{46}$$

Using this relationship, the force acting on the boulder from the vehicle is simply:

$$F_v = -m_v \ddot{x}_v \tag{47}$$

In the event of a vehicular rebound and separation, the vehicle cannot "pull" on the boulder. This discontinuity is handled by enforcing a constraint that any negative force at the contact is set to zero.

To model the moment imparted on the boulder by the vehicular impact, consider Equation (48).

$$M_v = F_v R_v \cos(\gamma_v + \theta_b) \tag{48}$$

As shown in Ref. [5], the spring and damper coefficients for a Maxwell model for a collision in which rebound is observed can be

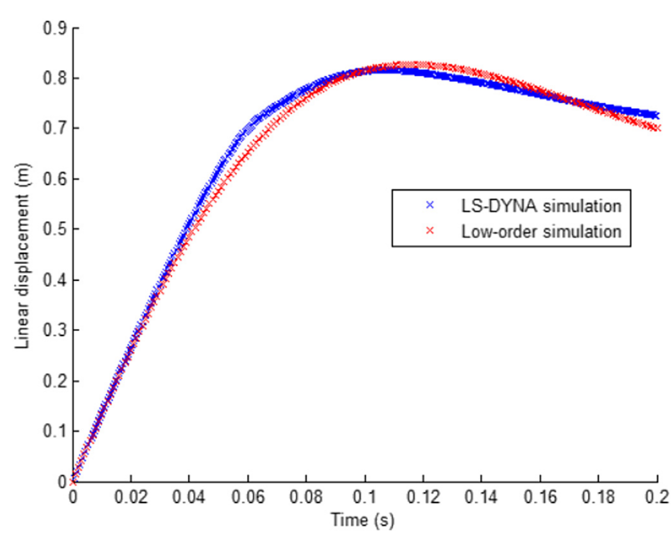

Fig. 10. Comparison of LS-DYNA® simulation to lumped-parameter Maxwell vehicle model.

Table 1
Low-order model parameters common to both tests.

$k_v = 3103.3\,\frac{kN}{m}$	$c_v = 138.91\,\frac{kN-s}{m}$	$N = 5000$

estimated by fitting an expected response to crash data. The expected response takes the form of Equation (49).

$$x_v = -\frac{2av_0}{a^2+b^2} + \exp\left[\left(\frac{v_0 - \frac{2a^2v_0}{a^2+b^2}}{b}\right)\sin(bt) + \frac{2av_0}{a^2+b^2}\cos(bt)\right] \tag{49}$$

Here, a and b are fitting constants, v_0 is the initial impact velocity of the vehicle, and t is time [5]. The constants a and b can then be correlated to the effective vehicle spring and damper coefficients as in Ref. [5], shown in Equations (50) and (51).

$$c_v = \frac{m_v(a^2+b^2)}{-2a} \tag{50}$$

$$k_v = -2ac_v \tag{51}$$

The calibration of each of these parameters is discussed shortly, but is, in general, an exercise in empirically fitting crash test data with simulation results.

The governing equations of motion for the boulder are derived by substituting the equations above for individual force and moment components into Equations (10) and (11) for simulation of a vehicle-boulder impact event. These equations can be rearranged in state-space form and solved using numerical integration techniques. The full set of state equations are shown in Equation (52) below in compact form.

$$\begin{aligned}
&x_1 = x_b \quad \dot{x}_1 = x_2\\
&x_2 = \dot{x}_b \quad \dot{x}_2 = \frac{1}{m_{\text{eff}}}\left[\sum_{n=1}^{N}\{F_n\} + F_v\right]\\
&x_3 = \theta_b \quad \dot{x}_3 = x_4\\
&x_4 = \dot{\theta}_b \quad \frac{1}{J_{\text{eff}}}\left[\sum_{n=1}^{N}\{M_n\} + M_v + M_R\right]\\
&x_5 = x_v \quad \dot{x}_5 = x_6\\
&x_6 = \dot{x}_v \quad \dot{x}_6 = x_7\\
&x_7 = \ddot{x}_v \quad \dot{x}_7 = -\frac{k_v}{c_v}x_7 - \frac{k_v}{m_v}x_6 + \frac{k_v}{m_v}[x_2 + x_4R_v\cos(\gamma_v + x_3)]
\end{aligned} \tag{52}$$

Equation (52) is a set of coupled, first-order, nonlinear, non-stiff ordinary differential equations that can be solved easily using the MATLAB® ODE45 function. This allows for quick and easy comparison of simulated boulder behavior during an impact and actual crash test data. The simulation is driven by an initial condition (the initial vehicle velocity v_0) and needs no other forcing functions or inputs. Each simulated impact takes less than one second to complete, even on a modestly powered laptop computer, allowing for quick design iterations to determine an appropriate boulder size for stopping a particular vehicle at a particular impact speed.

While the equations above represent only the most significant contributors to the gross vehicle and soil motion observed during a crash test, and high-order effects like vehicle crush nonlinearity and high-order vehicle and soil vibrations are ignored, the model is shown in the next section to be sufficiently accurate for

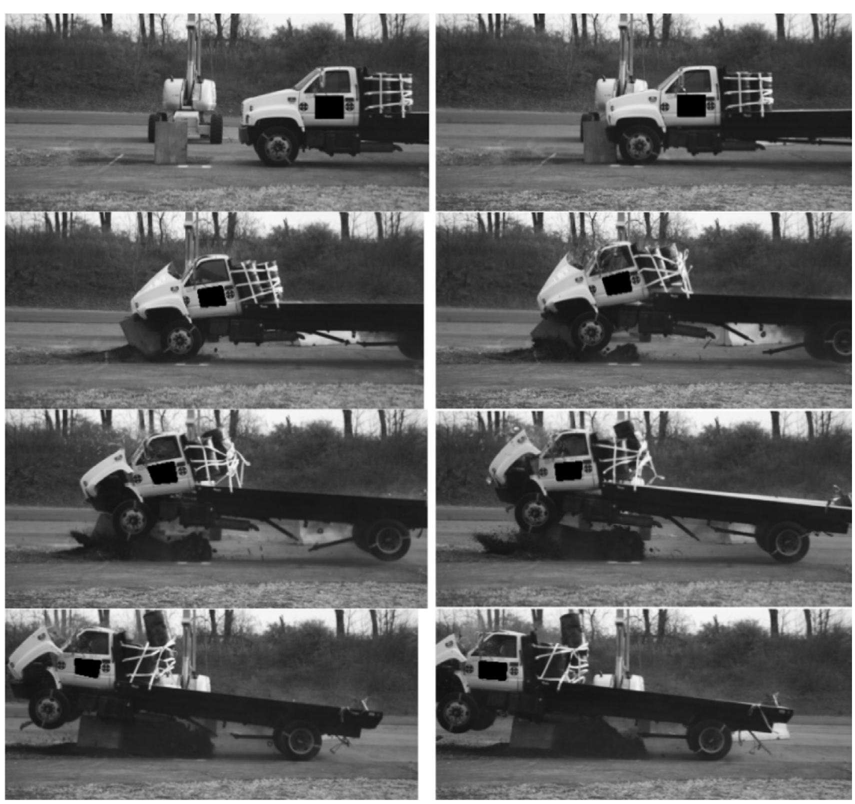

Fig. 11. Image sequence from American Black Granite boulder crash.

Table 2
Governing parameters for the American Black Granite test.

$\rho_{soil} = 1859.9\ \frac{kg}{m^3}$	$H = 2.2$ m	$\beta = 95\ \frac{MN}{m^3}$
$\rho_b = 3074\ \frac{kg}{m^3}$	$d = 1.2$ m	$e = 0.754$ m
$L = 0.762$	$m_v = 6795$ kg	$\phi' = 43.2°$
$W = 1.016$	$v_0 = 13.36\ \frac{m}{s}$	

determining whether a barrier will result in small enough boulder motion to guarantee a “pass” rating in a crash.

3. Validation of low-order model

For comparison with results from the low-order model developed in the preceding section, two full-scale crash tests were performed at an M30 (30 mph) rating as specified in ASTM F2656-07 under the supervision of the Penn State Crash Safety Research team at the Larson Transportation Institute.

3.1. Test setup

The institute's Crash Safety Research Facility uses a guide rail system for steering the impact vehicle, a reverse towing system for accelerating the impact vehicle up to the desired speed, and a cable release device for separating the tow cable from the impact vehicle just prior to the crash. The facility is shown in Fig. 7. The guide rail is approximately 320 m long, with a bogey catch attached to the end closest to the impact site that serves as the tow cable release device. Fig. 8 shows a symbolic layout of the guide rail and tow system. The tow system shown in Fig. 8 consists of a tow vehicle, tow cable, redirection pulleys, and a speed multiplier pulley, which allows the tow vehicle to travel at half the speed of the impact vehicle.

The soil surrounding the boulder in both of the crash tests performed for this study was 2 A modified limestone gravel. The gravel was compacted using a hydraulic tamper according to ASTM F2656-07 standards.

The primary data acquisition system used for full scale crash tests as related to this research was a set of three Photron Ultima 1024 high-speed imaging systems. The first Ultima 1024 was located at a 90° angle from the side of the impact vehicle 20.5 m away from the boulder's center, capturing the crush of the vehicle and translation and rotation of the boulder. The second camera was located directly above the test article facing downward for a plan view at a height of 15.9 m, and the third was located 32.2 m beyond the crash site along the guide rail facing opposite the direction of the test vehicle's travel direction. This setup is shown diagrammatically in Fig. 9.

For the tests in this study, each camera was set to record 500 frames per second for 2 s after receiving a trigger signal. The trigger system consisted of two reflective laser beams used to determine when the impact vehicle passes through the trigger point. When both laser beams are broken, a TTL signal is sent to the high-speed camera which initiates recording. The high-speed video data from the crash were processed to extract boulder and vehicle translation and rotation using the automated fiducial tracking algorithm available in the Photron Motion Tools software. The speed of the towed crash vehicle was controlled by the tow vehicle driver using a Stalker Speed Sensor (S3) radar system.

For each test discussed below, the constant of horizontal subgrade reaction β for the limestone gravel was obtained from tabular data to be 95 $\frac{MN}{m^3}$ at 90% maximum density, a criterion for the ASTM

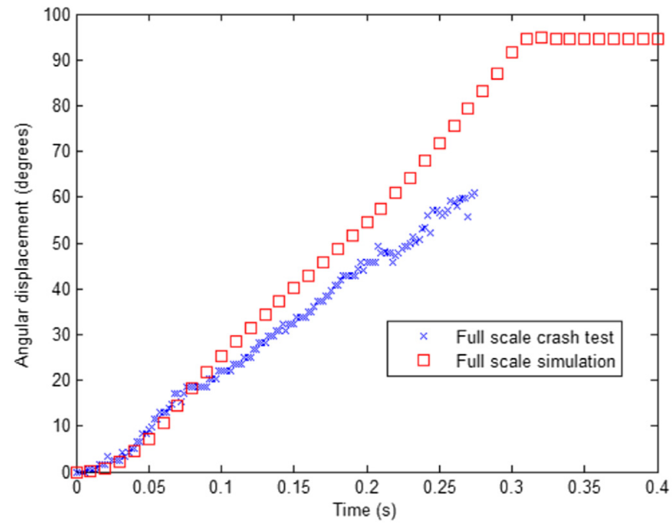

Fig. 13. Comparison of the measured and simulated rotation of the American Black Granite boulder.

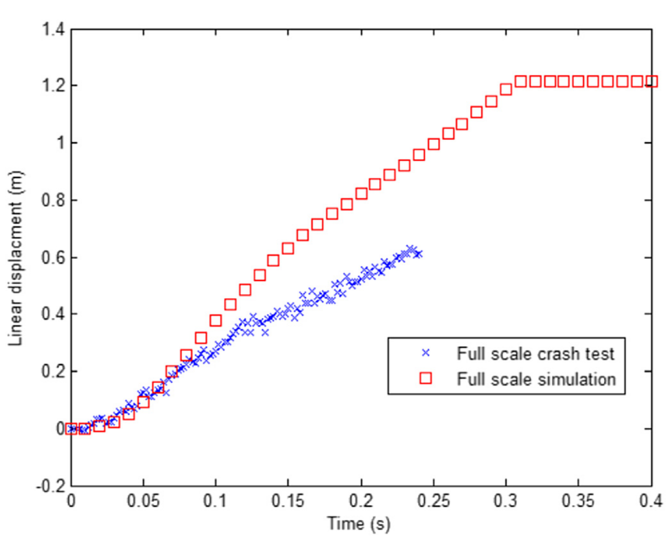

Fig. 12. Comparison of the measured and simulated displacement of the center of mass of the American Black Granite boulder.

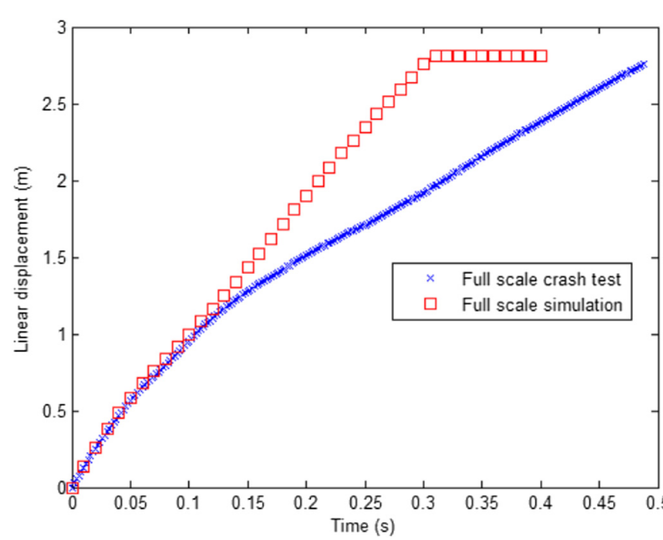

Fig. 14. Comparison of the measured and simulated displacement of the vehicle during the American Black Granite boulder test.

Table 3
Governing parameters for the Rockville White Granite test.

$\rho_{soil} = 1859.9\ \frac{kg}{m^3}$	$H = 3.44$ m	$\beta = 95\ \frac{MN}{m^3}$
$\rho_b = 2596\ \frac{kg}{m^3}$	$d = 2.03$ m	$e = 0.938$ m
$L = 1.65$	$m_v = 6722$ kg	$\phi' = 43.2^\circ$
$W = 1.68$	$v_0 = 14.5\ \frac{m}{s}$	

F2656-07 test protocol. A modified proctor test was performed to obtain the soil density as 2010 $\frac{kg}{m^3}$. The density of American Black Granite and Rockville White Granite were measured to be 3074 $\frac{kg}{m^3}$ and 2652 $\frac{kg}{m^3}$ respectively.

The measured angular and linear displacements of the boulder in the actual crash tests were made with respect to the boulder's center of mass using a set of fiducial stickers. In the low-order simulation, however, the output is of the boulder-soil subsystem's center of mass. These two quantities can be related using Equation (53).

$$x'_b = x_b + R'_b \cos(\gamma'_b - \theta_b) \tag{53}$$

where R'_b is the radial distance from the boulder-soil subsystem's center of mass to the boulder's center of mass, and γ'_b is the angle measured from the positive X-direction to the boulder's center of mass. R'_b and γ'_b are given by Equation (54) and Equation (55) respectively.

$$R'_b = \sqrt{\left(c_x - \frac{L}{2}\right)^2 + \left(c_y - \frac{H}{2}\right)^2} \tag{54}$$

$$\gamma'_b = \arctan\left(\frac{c_x - \frac{L}{2}}{c_y - \frac{H}{2}} + \frac{\pi}{2}\right) \tag{55}$$

The number of elements in the low-order model, N, was increased until the model outputs converged between successive simulation runs. Simulation results are sensitive to changes in the number of soil elements for small N, but showed no change for increasing N above 5000 elements. Therefore, the simulation results summarized below both used $N = 5000$.

3.2. Determination of Maxwell model vehicle parameters

The low-order simulations in the comparisons with crash tests below are performed by first parameterizing a typical medium-duty sized truck in terms of an equivalent spring and damper constant for use in the Maxwell vehicle model. The equivalent spring and damping values for the low-order vehicle are found using the methodology presented in Ref. [5]. An LS-DYNA® finite element simulation was performed by Larson Institute personnel for a medium-duty sized truck traveling at 13.4 $\frac{m}{s}$ impacting a rigid wall. The fit achieved for the spring and damper constants, found to be 3103 $\frac{kN}{m}$ and 138.91 $\frac{kN-s}{m}$ respectively, is shown in Fig. 10.

As Fig. 10 shows, after fitting, the Maxwell model describes the vehicle motion during a rigid wall impact very well. Therefore, the equivalent spring and damper constants obtained from the rigid wall impact simulation using LS-DYNA were used in the low-order model simulations to approximate the vehicle's spring and damper properties during the boulder impact. Table 1 summarizes the vehicle and element constants for simulation that remained constant for both tests.

3.3. American Black Granite boulder test results

The first test performed, a 29.9 mph impact by a Chevrolet C6500 medium-duty truck loaded to a total weight of 15,000 lb using ballast barrels into an American Black Granite boulder of dimensions 0.762 m–L × 1.016 m–W × 2.2 m–H with respect to the impact direction, resulted in very large movement of the boulder and penetration of the barrier by the impact vehicle. The boulder was embedded 1.2 m into the soil. An image sequence taken from the high-speed video is shown in Fig. 11.

Based on the stationary radar system and confirmed by analysis of the high-speed video, the approach speed at impact was 13.4 $\frac{m}{s}$ or 29.9 mph. Parameters used for simulation of the low-order model equations are shown in Table 2.

The match between the low-order model predictions of displacement and the collected data from the crash is shown in Fig. 12. As Fig. 12 shows, the model match is very close until approximately 0.1 s. The cause for the disagreement between the simulation and the collected data after this point is likely due to the large angular displacement of the boulder, which, as Fig. 11 shows,

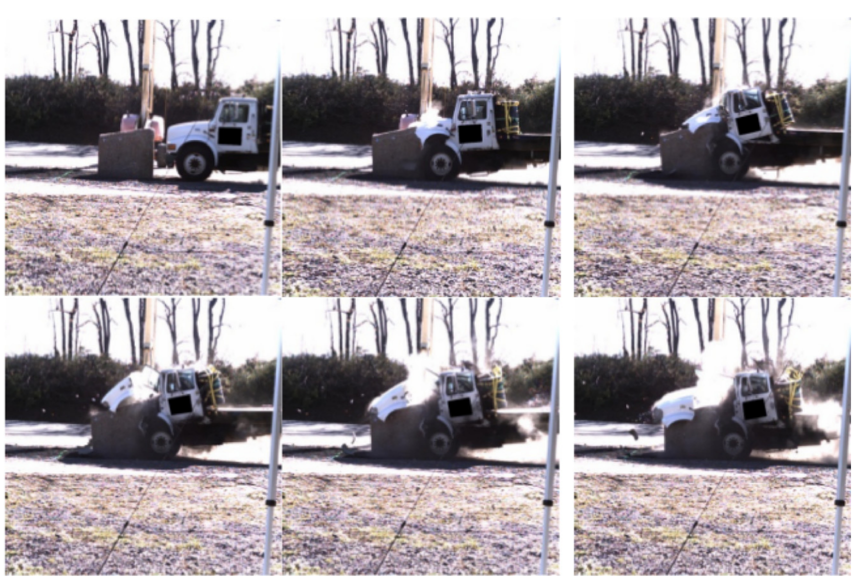

Fig. 15. Image sequence from Rockville White Granite boulder crash.

"flipped" up and out of the ground during the test, violating many assumptions of the model, including zero *Y*-displacement of the boulder. Corroborating this hypothesis, Fig. 13 shows the comparison between simulated and collected boulder rotation angle. Again, for small displacements, the model matches the physical experiment, but results for boulder angular displacement diverge after a rotation of 20°. Finally, the same trend is exhibited in the comparison of predicted vs. measured vehicle motion, shown in Fig. 14. It appears, then, that the low-order model's utility is limited to boulders that are large enough to maintain small motions when impacted. Because the goal of the model itself is to determine whether a boulder can stop a vehicle, this is an acceptable constraint. Simulations of impacts in which large boulder motion is predicted (above 20° rotation) should not be considered candidates for using the boulder as an effective barrier due to the increased chances of a truck ramping over the boulder. To determine whether the model predicts boulder and vehicle motion more accurately for impacts that exhibit relatively small predicted motions, the low-order model was used to simulate an impact with a Rockville White Granite boulder of considerably larger dimension.

3.4. Rockville White Granite boulder test

The Rockville White Granite boulder selected for the second test was chosen with dimensions that represented the maximum installable weight for the Larson Institute Crash Safety Research Center. The boulder was embedded 2.03 m in the soil. The vehicle used in the test was a 1999 International 4700 medium-duty truck, and was prepared as specified in ASTM F2656-07. Additional ballast was once again added to the front of the truck bed in order to achieve a total weight of 6722 kg or 14,820 lb. The boulder translated and rotated slightly on impact, and the front of the truck rebounded after impact. The test was deemed a "pass" according to ASTM standards, and the vehicle did not penetrate.

The governing parameters for the test are shown in Table 3 and a sequential image sequence from the test is shown in Fig. 15. As expected, the much larger boulder moved considerably less than the smaller American Black Granite specimen.

The match between the low-order model predictions of displacement and the collected data from the crash is shown in Fig. 16. In Fig. 16, the model match for the Rockville White Granite test was significantly improved for the duration of the test when

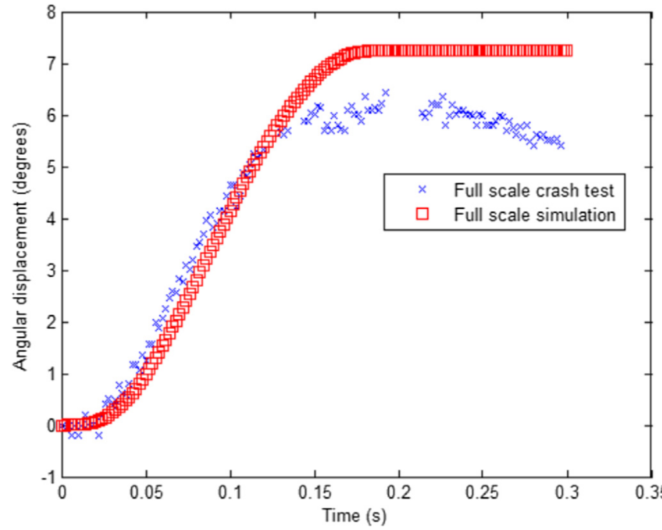

Fig. 17. Comparison of the measured and simulated rotation of the Rockville White Granite boulder.

compared to the American Black Granite test, a function of increased boulder dimensions and mass. The boulder rotation angle agreement, shown in Fig. 17, was also significantly improved.

Because the overall motion of the boulder was smaller, the rotation angle predicted by the model agrees with collected data.

Finally, the vehicle motion agreed for the second test as well and is shown in Fig. 18. The predicted and simulated vehicle motion values match well while vehicle motion is small, but nonlinearities and increasing stiffness of the vehicle chassis with a large amount of vehicular crush make the results diverge after about 1 m of displacement. Recall that the Maxwell model for vehicle motion is linear, while the actual vehicle behavior is not.

4. Discussion

The goal of this study was to develop and validate a low-order model for motion of the vehicle-boulder system that predicted boulder and vehicle motion to a degree that allows for the model's

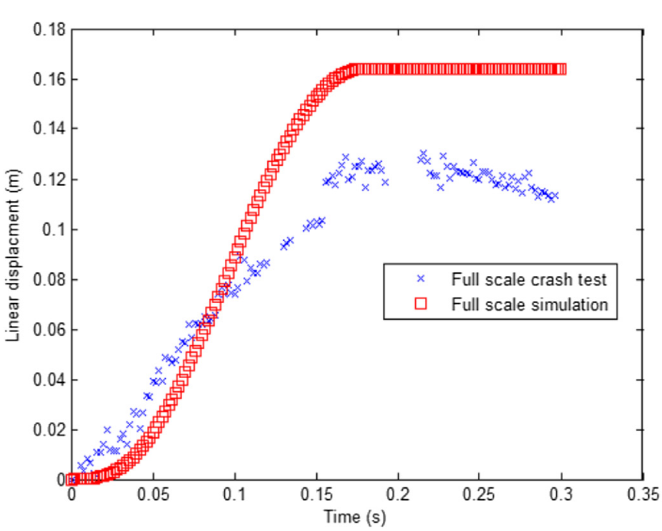

Fig. 16. Comparison of the measured and simulated displacement of the center of mass of the Rockville White Granite boulder.

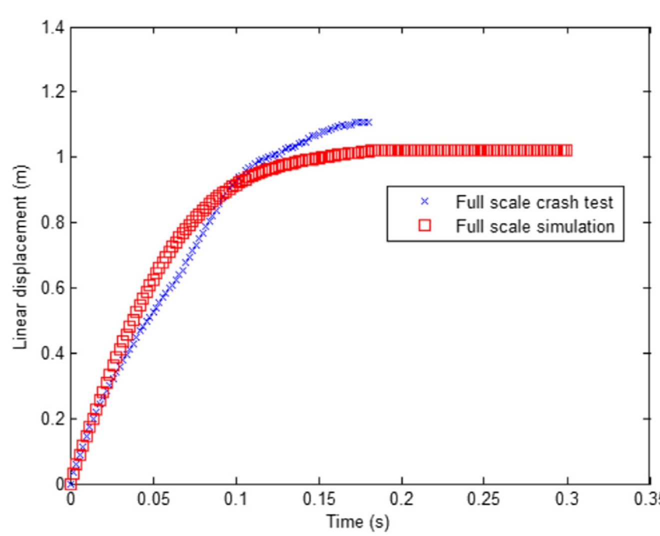

Fig. 18. Comparison of the measured and simulated displacement of the vehicle during the Rockville White Granite boulder test.

use in selecting boulder dimensions for a specific impact criterion, or for determining whether an existing soil-embedded boulder could serve as an effective vehicular barrier. The results of the first test on the smaller American Black Granite boulder indicate that the model is not suitable for tests where large rotations are predicted. For the second test using the larger Rockville White Granite boulder, the model match improved dramatically because boulder motion was significantly smaller. The simulated displacements were conservative for this test for boulder rotation and translation, which is an acceptable result when the goal is to design a system that limits vehicle motion. The overestimation in numerical simulation for boulder rotation and translation can be attributed to various assumptions made in our formulations. In particular, the equations neglect of strain rate effect on soil resistance (see Equation (27)). Unlike boulder motion, Vehicle motion was not conservative. However, the model match is close considering that the impact model for the vehicle was linear.

Despite the expense of conducting full-scale crashes for validation, these two tests showed that the model is functional for scenarios where small displacements are likely, and can accurately predict a "passing" and "failing" boulder configuration as per ASTM 2656-07 testing protocol. Thus, the model was deemed suitable for use in selecting boulder dimensions to resist impacts by medium-duty trucks at an M30 rating.

5. Conclusions

This paper presented a detailed derivation of a low-order model for predicting the motion of a vehicle-boulder impact. The model is based on first-principles, and can be modeled using coupled nonlinear, first-order differential equations. The soil's reaction forces on the boulder were modeled by discrete soil elements whose motion was linked kinematically to the rigid body motion of the boulder, keeping the system equations simple. Two full-scale physical tests were conducted using boulders of disparate size to assess the fidelity of the model across test conditions. The low-order model was found to be satisfactorily descriptive and accurate for analyzing impacts with boulder rotations under 20°.

Acknowledgments

The authors would like to thank the United States Department of State (Grant no. DSPPSP-10-CA-WHA-052110) and the Larson Transportation Institute for their continuing support of this research.

References

[1] Atahan AO. Vehicle crash test simulation of roadside hardware using ls-dyna: a literature review. Int J Heavy Veh Syst 2010;17(1):52–75.
[2] Sennah K, Samaan M, Elmarakbi A. Impact performance of flexible guardrail systems using LS-DYNA. In: 4th European LS-DYNA Users Conference. ULM, Germany: DYNAmore GmbH; 2003. p. 35–43.
[3] Wu W, Thomson R. A study of the interaction between a guardrail post and soil during quasi-static and dynamic loading. Int J Impact Eng 2007;34(5): 883–98.
[4] Hu B, Li Gq, Sun Jy. Numerical investigation of K4-rating shallow footing fixed anti-ram bollard system subjected to vehicle impact. Int J Impact Eng 2014;63:72–87.
[5] Pawlus W, Karimi HR, Robbersmyr KG. Development of lumped-parameter mathematical models for a vehicle localized impact. J Mech Sci Technol 2011;25(7):1737–47.
[6] Pawlus W, Karimi HR, Robbersmyr KG. Mathematical modeling of a vehicle crash test based on elasto-plastic unloading scenarios of spring-mass models. Int J Adv Manuf Technol 2011;55(1–4):369–78.
[7] Pawlus W, Reza H, Robbersmyr KG. Application of viscoelastic hybrid models to vehicle crash simulation. Int J Crashworthiness 2011c;16(2):195–205.
[8] Karimi HR, Robbersmyr KG. Signal analysis and performance evaluation of a vehicle crash test with a fixed safety barrier based on haar wavelets. Int J Wavelets Multiresolution Inf Process 2011;9(01):131–49.
[9] Pawlus W, Robbersmyr KG, Karimi HR. Mathematical modeling and parameters estimation of a car crash using data-based regressive model approach. Appl Math Model 2011d;35(10):5091–107.
[10] Zhang L. Nonlinear analysis of laterally loaded rigid piles in cohesionless soil. Comput Geotech 2009;36(5):718–24.
[11] El Naggar M, Bentley KJ. Dynamic analysis for laterally loaded piles and dynamic py curves. Can Geotech J 2000;37(6):1166–83.
[12] Novak M, Sheta M. Approximate approach to contact effects of piles. In: Dynamic response of structures: experimentation, observation, prediction and control. New York, New York: ASCE; 1980. p. 53–79.
[13] Hesham El, Naggar M. Interpretation of lateral statnamic load test results. ASTM Geotech Test J 1998;21(3):169–79.
[14] Kim Y, Jeong S, Lee S. Wedge failure analysis of soil resistance on laterally loaded piles in clay. J Geotech Geoenviron Eng 2010;137(7):678–94.
[15] Murchison J, O'Neill M, Meyer JR, editors. Evaluation of P-Y relationships in cohesion less soils. Analysis and design of pile foundations. San Francisco, California: ASCE; 1984. p. 174–91.
[16] Terzaghi K, Peck R, Mesri G. Soil mechanics in engineering practice. New York, New York: Wiley. Com; 1996. p. 246–50.
[17] Fleming K, Weltman A, Randolph M, Elson K. Piling engineering. New York, New York: Taylor & Francis; 2008. p. 145–55.
[18] Zhang L, Silva F, Grismala R. Ultimate lateral resistance to piles in cohesionless soils. J Geotech Geoenviron Eng 2005;131(1):78–83.
[19] Guo WD. Laterally loaded rigid piles in cohesionless soil. Can Geotech J 2008;45(5):676–97.
[20] Yamamuro JA, Abrantes AE, Lade PV. Effect of strain rate on the stress-strain behavior of sand. J Geotechn Geoenviron Eng 2011;137(12):1169–78.
[21] Seed Harry Bolton, Lundgren R. Investigation of the effect of transient loading on the strength and deformation characteristics of saturated sands. In: Proceedings-American Society for Testing and Materials vol. 54. 100 Barr Harbor Dr, W Conshohocken, PA 19428–2959: Amer Soc Testing Materials; 1954.
[22] Seed HB, Dunlop P, Lee KL. Effect of transient loading on the strength of sand. In: Proceedings of the 7th Conference on soil Mechanics and Foundation engineering, Mexico City, Mexico, vol. 1. Sociedad Mexicana de Mecanica de Suelos; 1969. p. 239–47.